Supplementary Information

Multimodal imaging and deep learning unveil pulmonary delivery profiles and acinar migration of tissue-resident macrophages in the lung

Lin Yang[1,2,]*, Qiongliang Liu[1,2,9], Pramod Kumar[1,2], Arunima Sengupta[1,2], Ali Farnoud[1,2], Ruolin Shen[3], Darya Trofimova[4,5], Sebastian Ziegler[4,5], Neda Davoudi[7,8], Ali Doryab[1,2], Ali Önder Yildirim[1,2], Herbert Schiller[1,2], Daniel Razansky[7,8], Marie Piraud[3], Gerald Burgstaller[1,2], Wolfgang G. Kreyling[1, 2, 6], Fabian Isensee[4,5], Markus Rehberg[1,2], Tobias Stoeger[1,2], Otmar Schmid[1,2]*

[1]Comprehensive Pneumology Center (CPC-M), Member of the German Center for Lung Research (DZL), Munich, 81377, Germany

[2]Institute of Lung Health and Immunity (LHI), Helmholtz Zentrum München - German Research Center for Environmental Health, Neuherberg, 85764, Germany.

[3]Helmholtz AI, Helmholtz Zentrum München, Munich, Germany

[4]Helmholtz Imaging, German Cancer Research Center (DKFZ), Heidelberg, Germany

[5]Division of Medical Image Computing, German Cancer Research Center (DKFZ), Heidelberg, Germany

[6]Institute of Epidemiology (EPI), Helmholtz Zentrum München - German Research Center for Environmental Health, Neuherberg, 85764, Germany

[7]Institute for Biomedical Engineering, Department of Information Technology and Electrical Engineering, ETH Zurich, Zurich 8093, Switzerland

[8]Institute of Pharmacology and Toxicology and Institute for Biomedical Engineering, Faculty of Medicine, University of Zurich, Zurich CH-8057, Switzerland

[9]Department of Thoracic Surgery, Shanghai General Hospital, Shanghai Jiao Tong University School of Medicine, Shanghai, China,

*Corresponding authors

Dr. Lin Yang

E-Mail: lin.yang@helmholtz-munich.de

Dr. Otmar Schmid

E-Mail: otmar.schmid@helmholtz-munich.de

Tel: +49-89-3187-2557. Fax: +49-89-3187-2400

Supplementary Information

Supplementary Figs. S1–S17 and Supplementary Videos and corresponding legends VS1-VS13.

Video legends:

Video S1: An exemplary holistic view of an INLA delivered lung with the manually annotation (ground truth) of lung airway.

Three-dimension (3D) co-mapping of lung morphology (green), INLA delivered NPs (red), manually annotated lung airway model (blue) in a whole mouse lung scanned by LSFM. Reference lung airway models (blue) were rendered in cyan. It depicts the lung shown in Figure 1d and Figure 3a.

Video S2: An exemplary holistic view of a NOAI delivered lung.

3D co-mapping of lung morphology (green) and NOAI delivered NPs (red) in a whole mouse lung scanned by LSFM (It depicts the lung shown in Figure 1e).

Video S3-1: 3D mapping of a 0h ITLI lung.

Co-visualization of NP distribution (red), lung geometry (green) and manually corrected AI airway segments (blue) in a mouse left lobe (Figure 2a).

Video S3-2: 3D mapping of a 2h ITLI lung.

Co-visualization of NP redistribution (red) and lung geometry (green) in a mouse left lobe (Figure 2b).

Video S3-3: 3D mapping of a 24h ITLI lung.

Co-visualization of NP redistribution (red) and lung geometry (green) in a mouse left lobe (Figure 2c).

Video S3-4: 3D mapping of a 14d ITLI lung.

Co-visualization of NP redistribution (red) and lung geometry (green) in a mouse left lobe (Figure 2d).

Video S4-1: 3D mapping of a 0h VAAD lung.

Co-visualization of NP distribution (red), lung geometry (green) and manually corrected AI airway segments (blue) in a mouse left lobe (Figure 2g).

Video S4-2: 3D mapping of a 2h VAAD lung.

Co-visualization of NP redistribution (red), lung geometry (green) and manually corrected AI airway segments (blue) in a mouse left lobe (Figure 2h).

Video S4-3: 3D mapping of a 24h VAAD lung.

Co-visualization of NP redistribution (red) and lung geometry (green) in a mouse left lobe (Figure 2i).

Video S4-4: 3D mapping of a 14d VAAD lung.

Co-visualization of NP redistribution (red) and lung geometry (green) in a mouse left lobe (Figure 2j).

Video S5: Exemplary active learning AI performance in common visible light channel.

An exemplary case of data-centric active learning AI method improving the segmentation performance of a full lung with out-of-center focus in the AF1 channel (ex/em=540/590, Figure 3b). Lung morphology (autofluorescence, AF1) in green, iterations 1, 3, and 6 from AF1 channels are in cyan, purple, and yellow, respectively.

Video S6: Exemplary active learning AI performance in near-infrared channel.

An exemplary case of data-centric active learning AI methodology improving the segmentation performance of a full lung with poor signal-to-noise ratio in the AF2 channel (ex/em=740/790 nm, Figure 3b). Lung morphology (autofluorescence AF2) in gray, iterations 1, 3, and 6 from AF2 channels are in cyan, purple, and yellow, respectively. Lung morphology in AF1 in green and corresponding iteration 6 in blue. VAAD delivered NPs in red.

Video S7: A perfect case of whole-lung airway segmentation.

This lung airway segmentation from the common visible light channel was obtained from our data-centric active learning AI model (Figure 3e_left). Lung morphology in green and iteration 6 in blue.

Video S8: Multiple localizations of macrophages in a 2h ITLI lung.

Cellular-resolution visualization of multiple locations of anti-F4-80^{+}, NP-laden macrophages particularly the ones located in interalveolar pores in 3D immunostained PCLS post 2h ITLI (Figure 4b). DAPI, anti-F4-80, podoplanin, and NPs as well as their corresponding surface renderings are in blue, green, cyan, and red, respectively.

Video S9: Multiple localizations of macrophages in a 2h VAAD lung.

Cellular-resolution visualization of multiple locations of anti-F4-80$^+$, NP-laden macrophages particularly the ones located in interalveolar pores in 3D immunostained PCLS post 2h VAAD (Figure 4b). DAPI, anti-F4-80, podoplanin, and NPs as well as their corresponding surface renderings are in blue, green, cyan, and red, respectively.

Video S10: Lung intravital microscopy of a 0h VAAD lung.

Lung intravital microscopy depicts the crawling dynamics of PKH$^+$NP$^+$ and PKH$^+$NP$^-$ macrophages in living mice for 2h immediately after VAAD delivery (PKH$^+$ cells in green, NPs in red, Figure 5a).

Video S11: *Ex-vivo* 4D living tissue microscopy of a 0h ITLI lung.

Ex-vivo 4D living tissue microscopy depicts the crawling behaviors of CSF1R-EGFP$^+$NP$^+$ and CSF1R-EGFP$^+$NP$^-$ macrophages in living lung sections (Figure 5b).

Video S12: Co-mapping of NP distribution with lung phagocytes.

Cellular resolution visualization of CSF1R-EGFP$^+$NP$^+$ and CSF1R-EGFP$^+$NP$^-$ macrophages in a whole-mount immunostained intact lung lobe. Macrophages in green and NPs in red (Figure 7a).

Video S13: Co-mapping of NP distribution with lung vasculature network.

Cellular resolution visualization of the vascular system (LYVE1$^+$) and NP distribution in a whole-mount immunostained intact lung lobe. LYVE1$^+$ vessels in green and NPs in red (Figure 7b).

Supplementary Figures

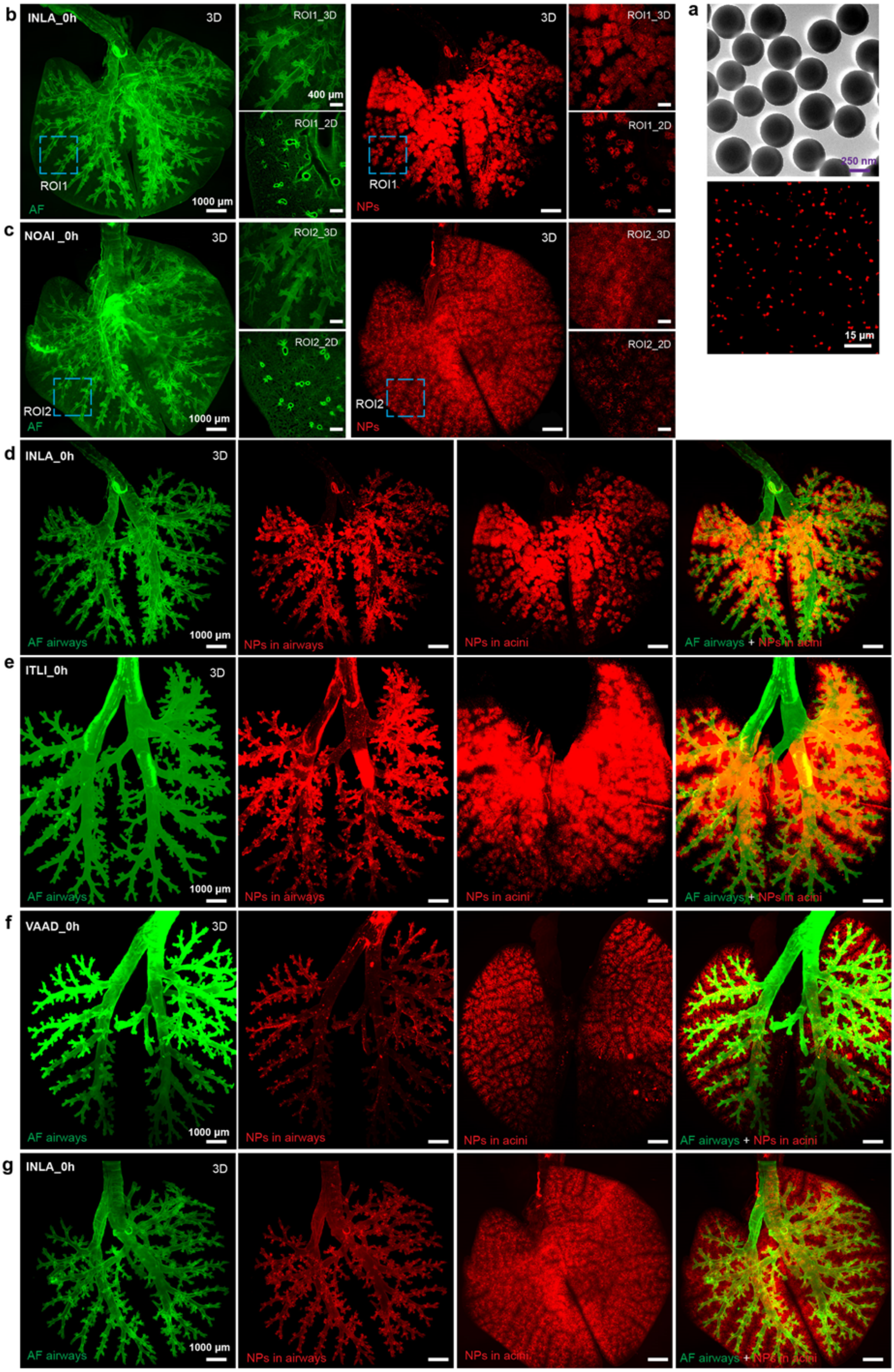

Figure S1: a) Characterization of MF NPs suspension using TEM and epi-fluorescence microscopy. b and c) 3D single channel view of lung morphology and particle distribution in lungs of mice immediately after intranasal liquid aspiration (INLA_0h) and nose-only aerosol inhalation (NOAI_0h). d-g) 3D views of only lung airways and NP distribution in airway and acini segmented from raw lung autofluorescence and NP channels for 4 routes of pulmonary delivery.

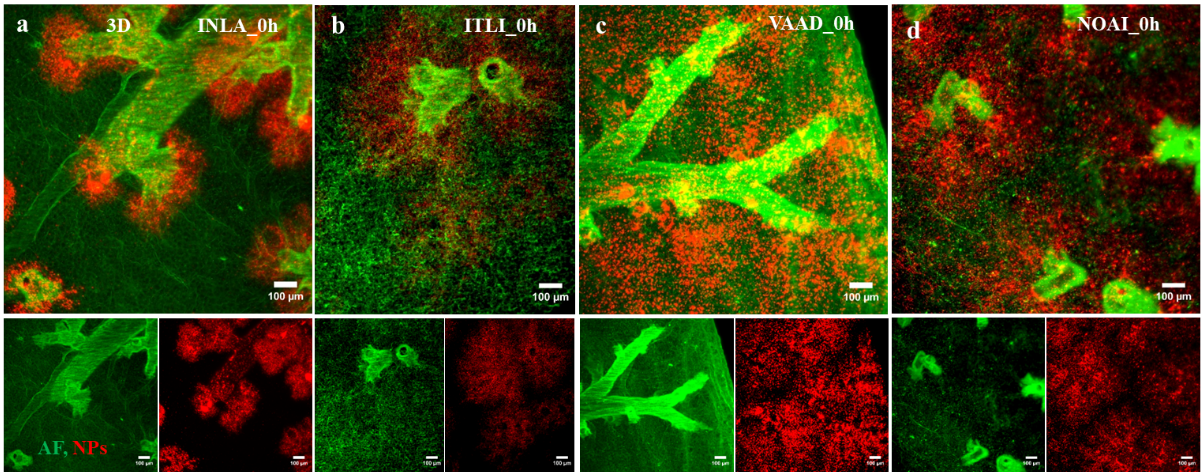

Figure S2: High-resolution 3D view of particle deposition patterns in the regions of smaller airway, terminal bronchioles, and proximal and distal acinar regions (PAR and DAR) for 4 types of delivery routes.

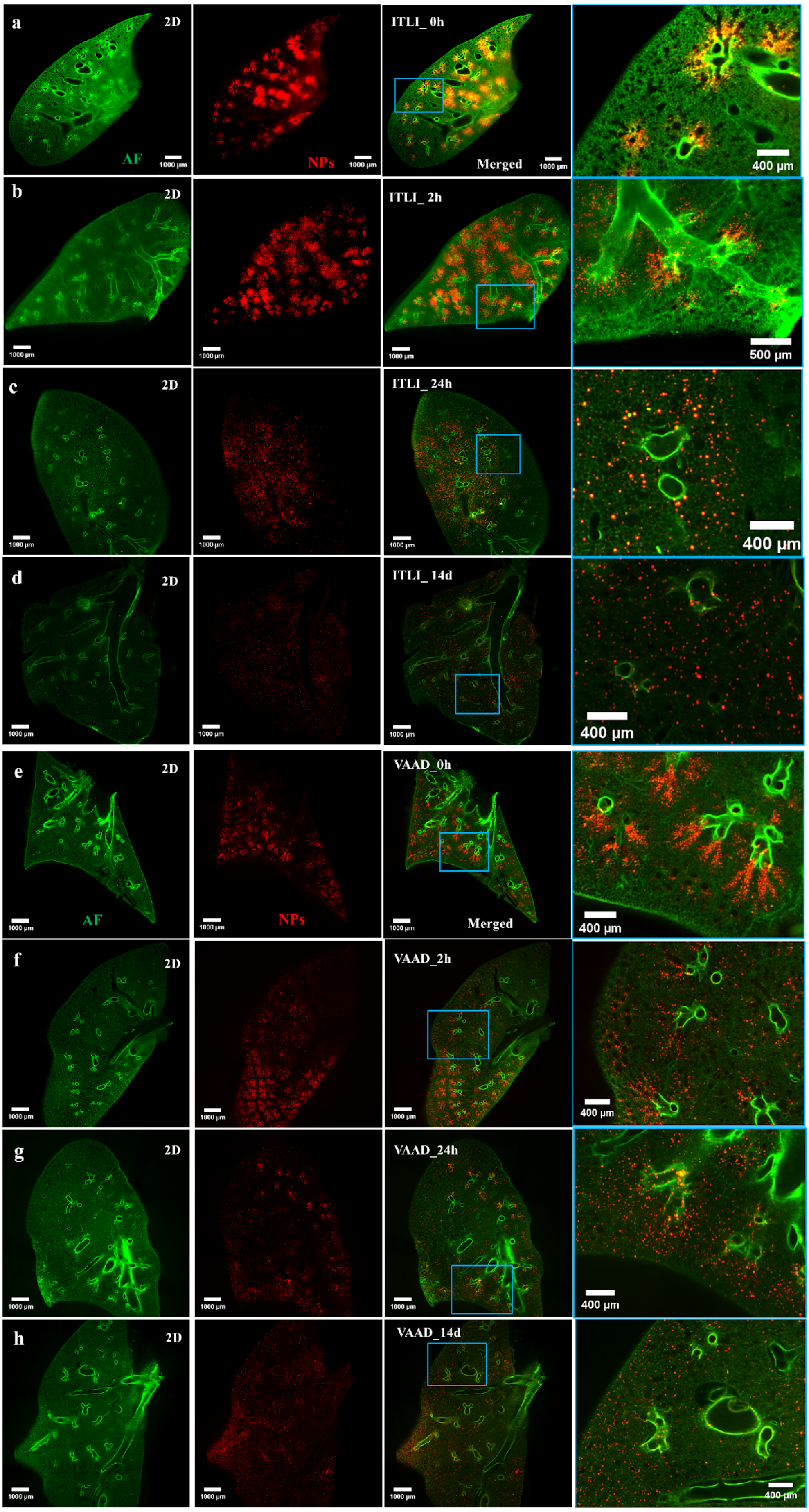
a
2D
AF
1000 µm
NPs
1000 µm
ITLI_ 0h
Merged
1000 µm
400 µm
b
2D
1000 µm
1000 µm
ITLI_ 2h
1000 µm
500 µm
c
2D
1000 µm
1000 µm
ITLI_ 24h
1000 µm
400 µm
d
2D
1000 µm
1000 µm
ITLI_ 14d
1000 µm
400 µm
e
2D
AF
1000 µm
NPs
1000 µm
VAAD_0h
Merged
1000 µm
400 µm
f
2D
1000 µm
1000 µm
VAAD_2h
1000 µm
400 µm
g
2D
1000 µm
1000 µm
VAAD_24h
1000 µm
400 µm
h
2D
1000 µm
1000 µm
VAAD_14d
1000 µm
400 µm

Figure S3: Single-slice (and merged) view of particle distribution pattern in mouse lungs over a time course ranging from 0h to 14d after intratracheal liquid instillation (ITLI, a-d) and ventilator-assisted aerosol delivery (VAAD, e-h).

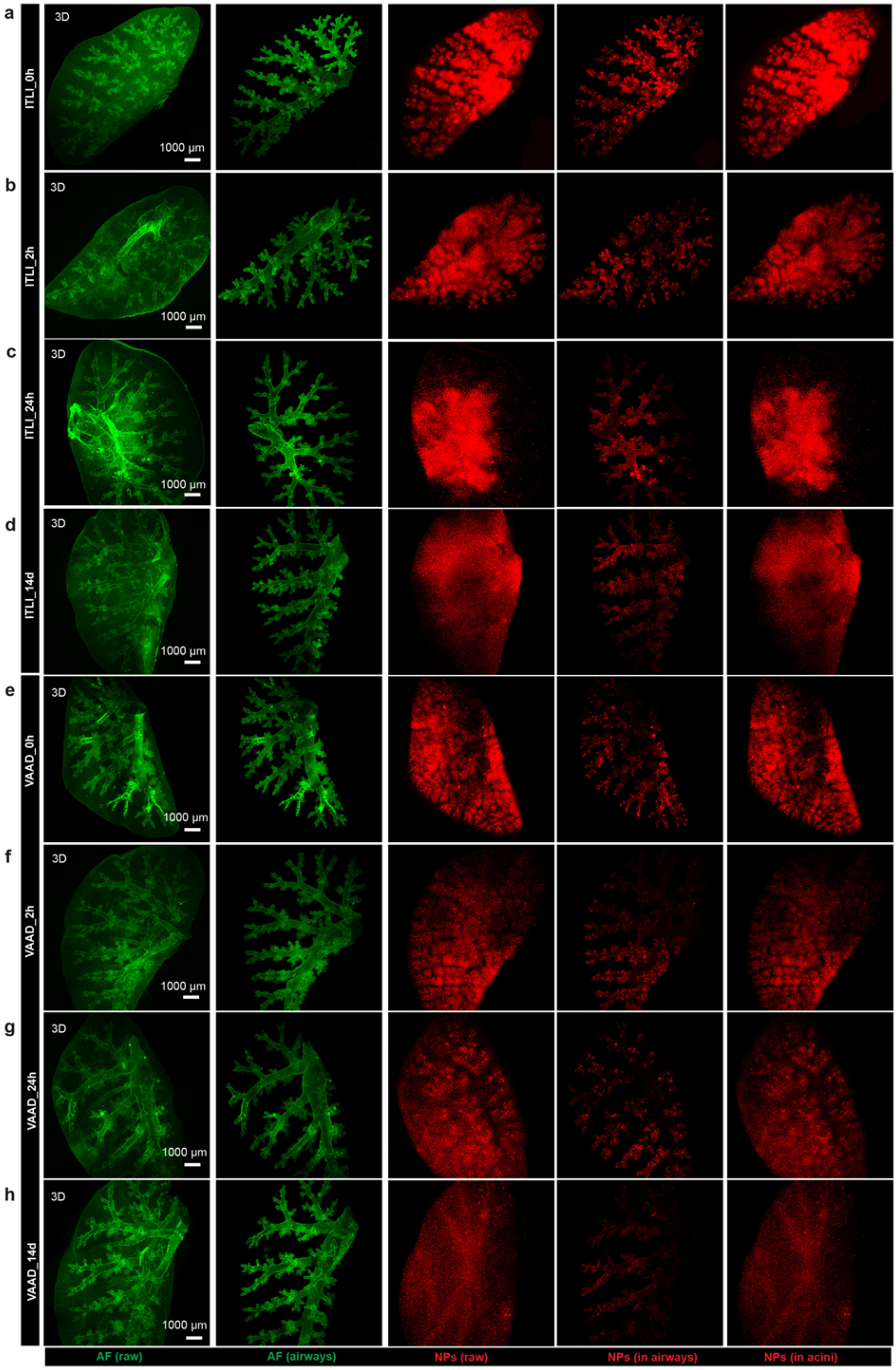
a
ITLI_0h
b
ITLI_2h
c
ITLI_24h
d
ITLI_14d
e
VAAD_0h
f
VAAD_2h
g
VAAD_24h
h
VAAD_14d
3D
1000 µm
AF (raw)
AF (airways)
NPs (raw)
NPs (in airways)
NPs (in acini)

Figure S4: Single-channel 3D view of separated lung airways (autofluorescence, AF) and NP distribution in lung airways or acini obtained from raw AF and NP channels, respectively.

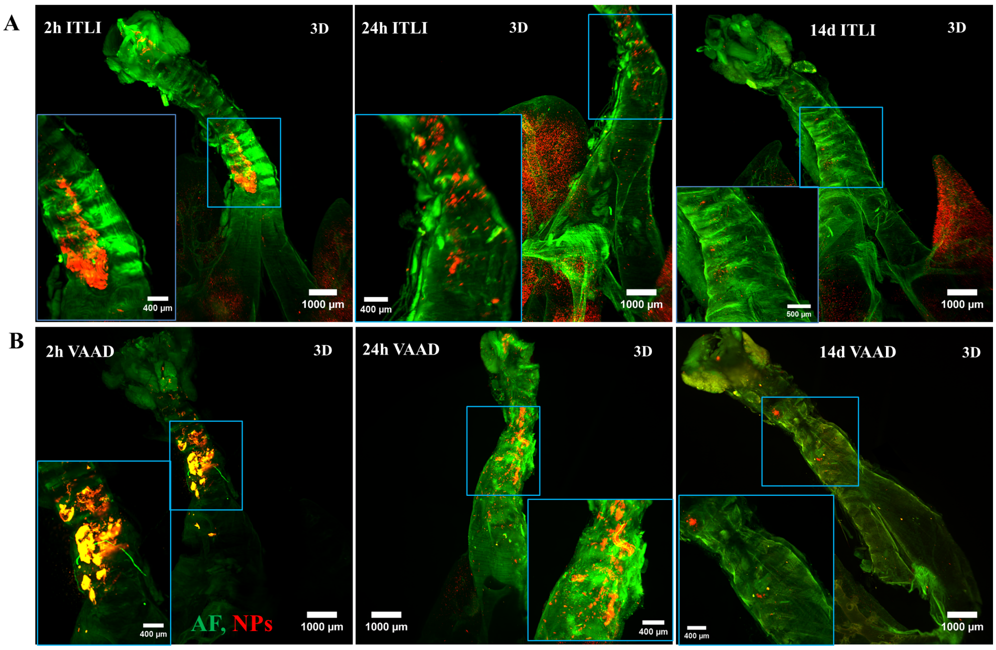

Figure S5: longitudinal observation of particle deposition and clearance in mouse trachea post ITLI and VAAD applications at time points of 2h, 24h, and 14d.

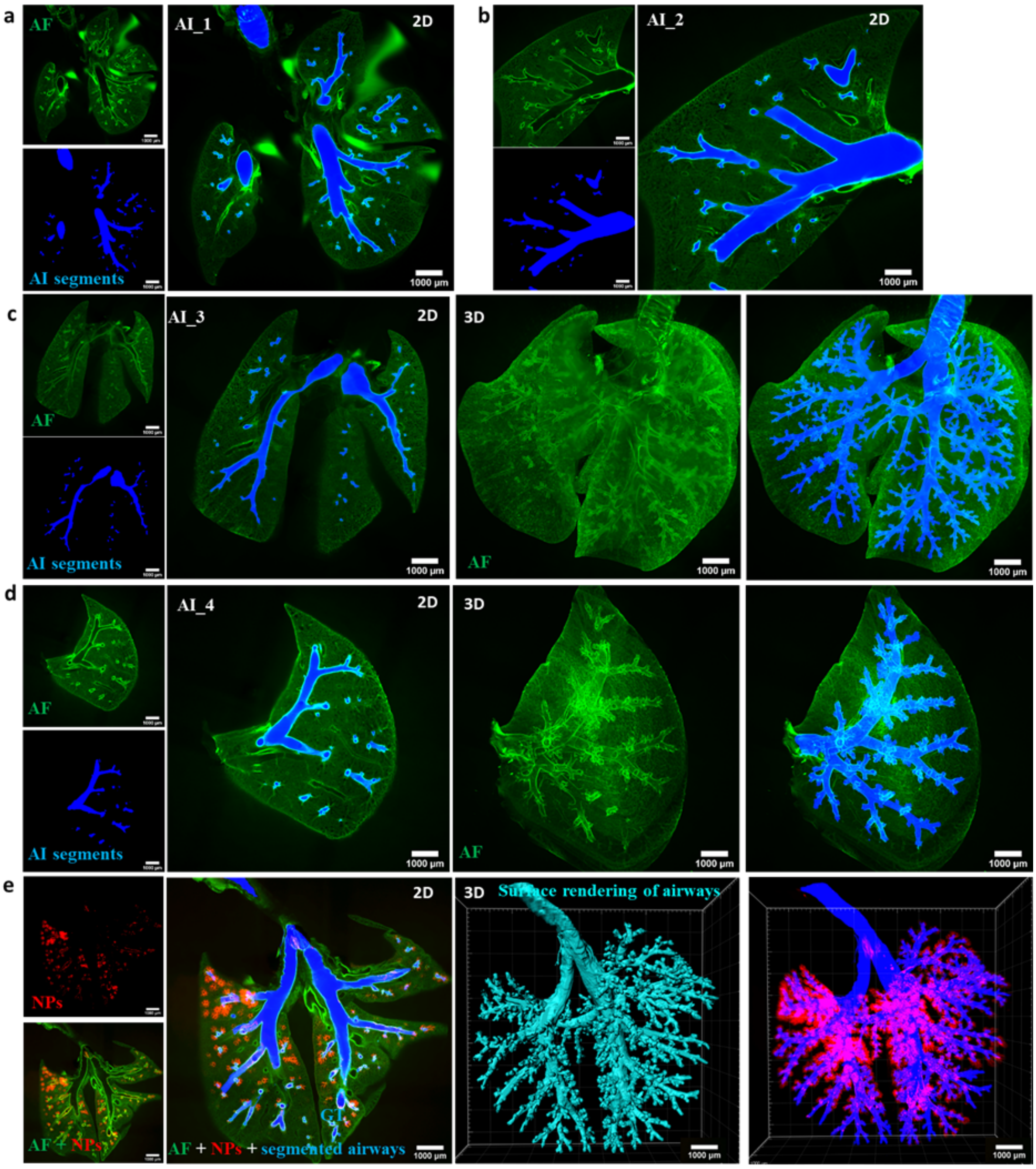

Figure S6: Exemplary AI segmented results of complete lung airways and methodological illumination for determination of B/A deposition ratio. a) and b) show representative 2D views of a whole-lung or a single lobe (the lungs displayed Figure 3c) with imaging artifacts like imaging shadow, obscure airways, and bright vessels. c) and d) display the excellent lung airway segmentations from the lungs with imaging artifacts such as blurring effects and uneven light illumination, which can be overcome by the data-centric active-learning AI approach. e) method demonstration of the concept of how to determine the bronchial NP dose and acinar NP dose.

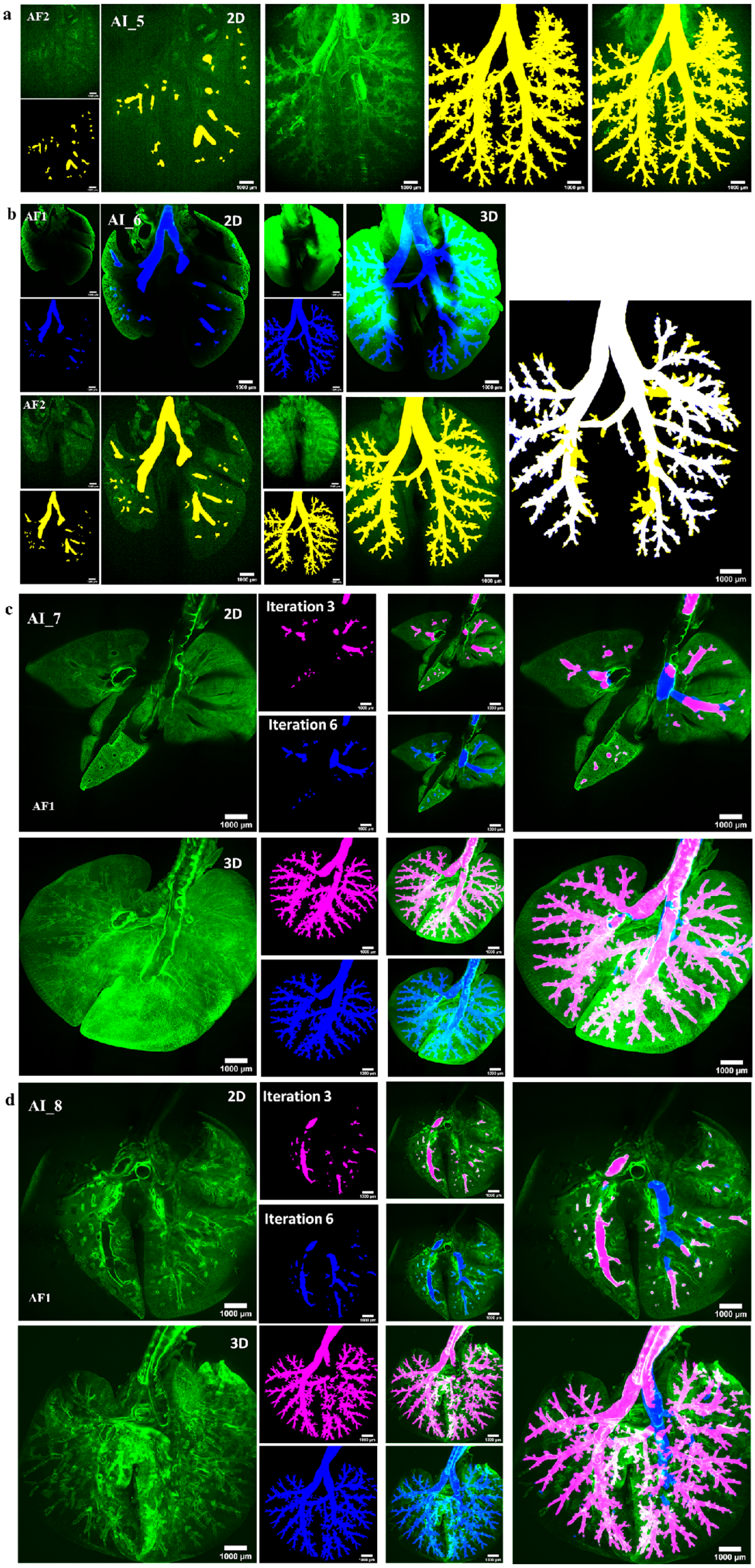
a
AF2
AI_5
2D
3D
1000 µm
b
AF1
AI_6
2D
3D
AF2
1000 µm
c
AI_7
2D
AF1
Iteration 3
Iteration 6
3D
1000 µm
d
AI_8
2D
AF1
Iteration 3
Iteration 6
3D
1000 µm

Figure S7: Active learning AI-driven approach achieved high-quality labeling of lung airways from specimens with different kinds of imaging artifacts. a) The lung specimen scanned in AF2 channel showed variable signal-to-noise ratio, air-bubble cased false structures, very weak fluorescence intensity, and unappreciated airways. b) Comparison of AI results generated from AF1 and AF2 channels in a lung sample with poor center illumination (dark regions) due to the blood residual, indicating the AF2 could gain better AI results due to less effects of blood effects or other imaging effects. c and d) the lung specimens displayed very bad imaging qualities like inconsistent illumination, obscure airways, false structures, and air-bubble caused gray structure, and active learning AI approach with more corrected samples and method improvement results in better labelling quality (better results for iteration 6 than 3).

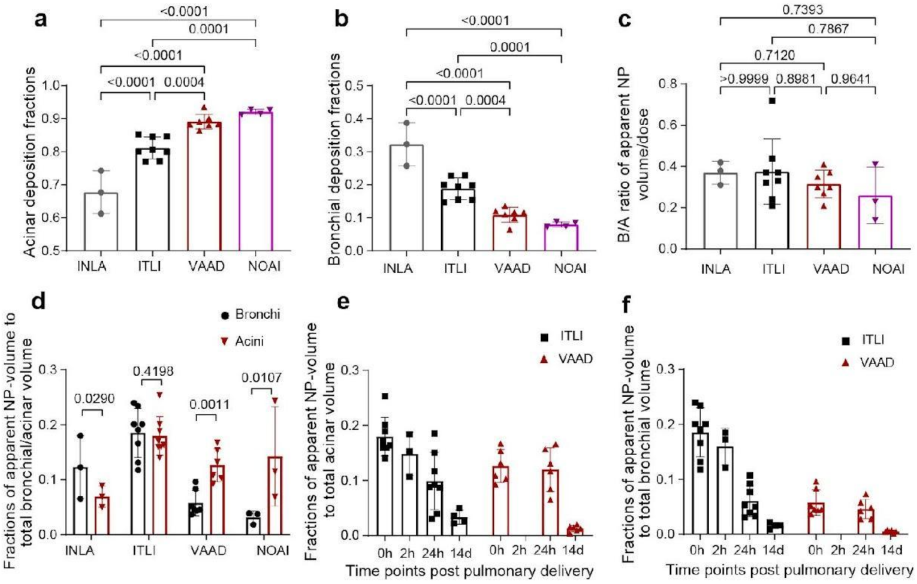

Figure S8: AI-assisted segmentation and quantification results on multiple new regional distribution profiles like acinar and bronchial deposition fractions (a and b), fractions of apparent NP-volume to total bronchial/acinar volume (c), and B/A ratio of apparent NP volume normalized to the dose (d) for all 4 types of application routes, as well as longitudinal fractions of apparent NP volume to total acinar or bronchial volume (e and f) over a time course of 14 days after VAAD and ITLI.

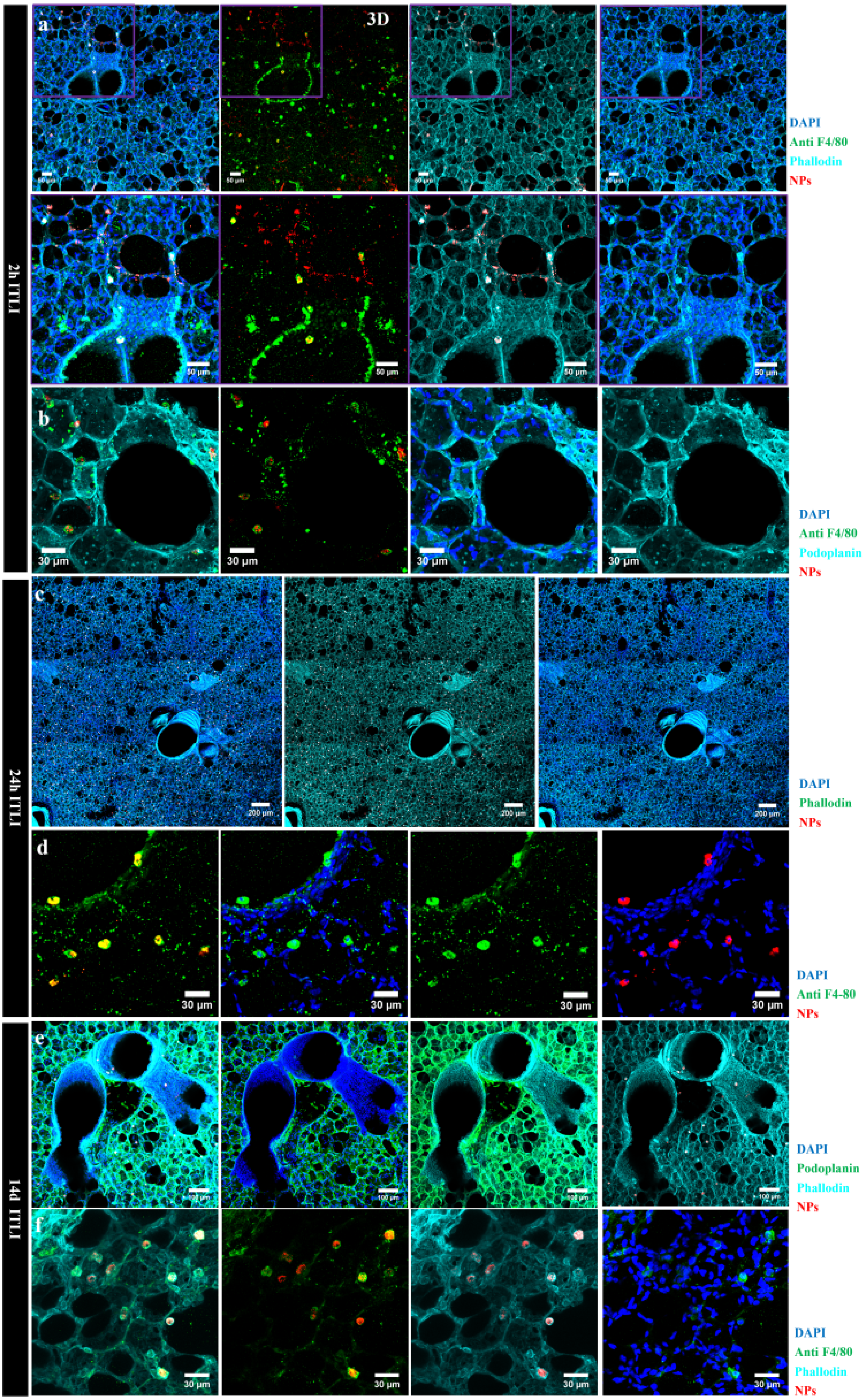
2h ITLI
24h ITLI
14d ITLI
a
3D
b
c
d
e
f
50 μm
30 μm
200 μm
100 μm
DAPI
Anti F4/80
Phallodin
NPs
DAPI
Anti F4/80
Podoplanin
NPs
DAPI
Phallodin
NPs
DAPI
Anti F4-80
NPs
DAPI
Podoplanin
Phallodin
NPs
DAPI
Anti F4/80
Phallodin
NPs

Figure S9: 3D view of acinar region with subcellular resolution of NP localization and cellular uptake (mainly F4-80$^+$ macrophages, TRMs) in PCLS using *in situ* immunofluorescence staining of mouse lungs after ITLI applications at time points of 2h, 24h, and 14d. Images show different combinations of fluorescent channels of stained antibodies or dyes.

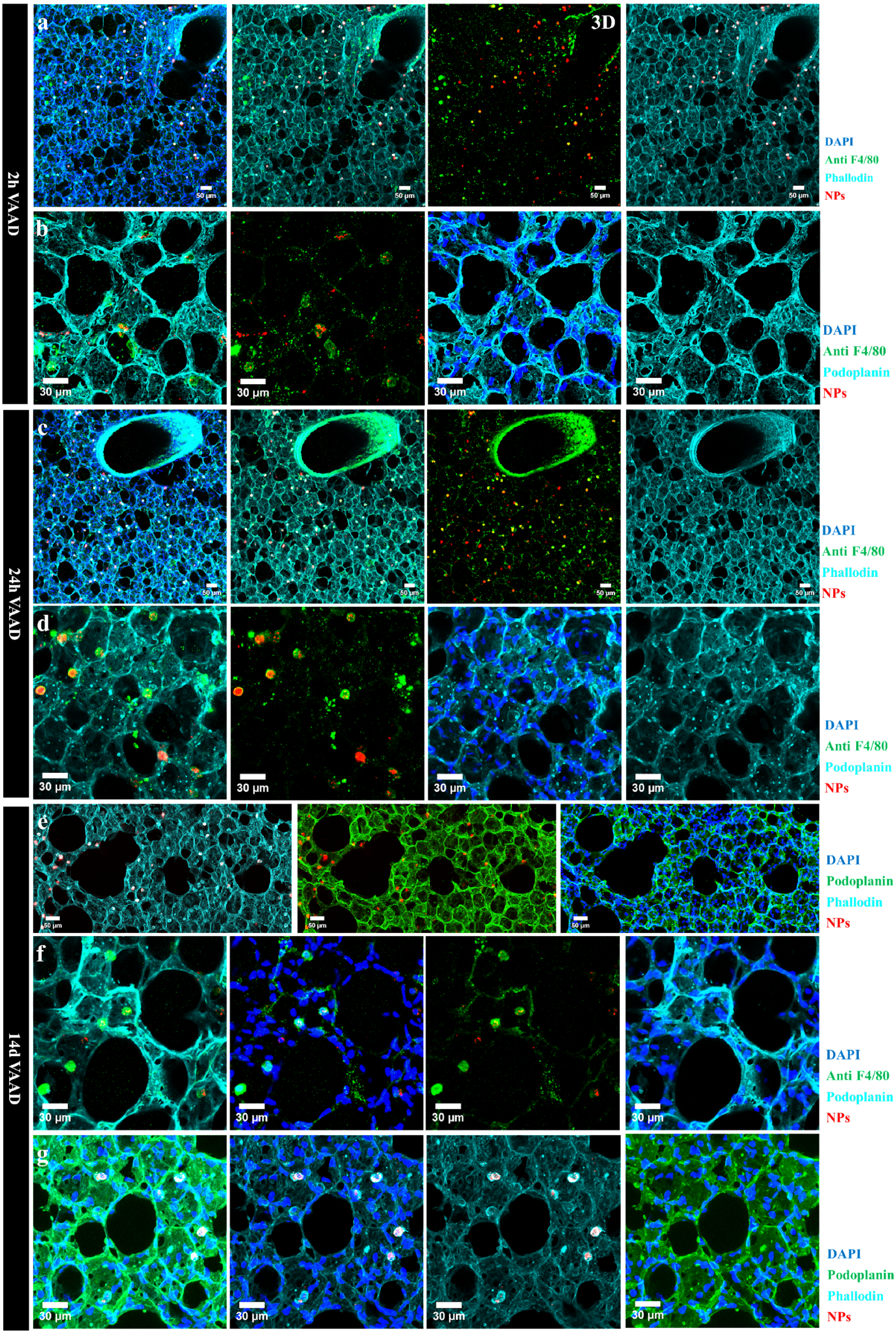
2h VAAD
a
3D
50 μm
DAPI
Anti F4/80
Phallodin
NPs
b
30 μm
DAPI
Anti F4/80
Podoplanin
NPs
24h VAAD
c
50 μm
DAPI
Anti F4/80
Phallodin
NPs
d
30 μm
DAPI
Anti F4/80
Podoplanin
NPs
14d VAAD
e
50 μm
DAPI
Podoplanin
Phallodin
NPs
f
30 μm
DAPI
Anti F4/80
Podoplanin
NPs
g
30 μm
DAPI
Podoplanin
Phallodin
NPs

Figure S10: 3D view of acinar region with subcellular resolution of NP localization and cellular uptake (mainly F4-80^{+} macrophages, TRMs) in PCLS using *in situ* immunofluorescence staining of mouse lungs after VAAD applications at time points of 2h, 24h, and 14d. Images show different combinations of fluorescent channels of stained antibodies or dyes.

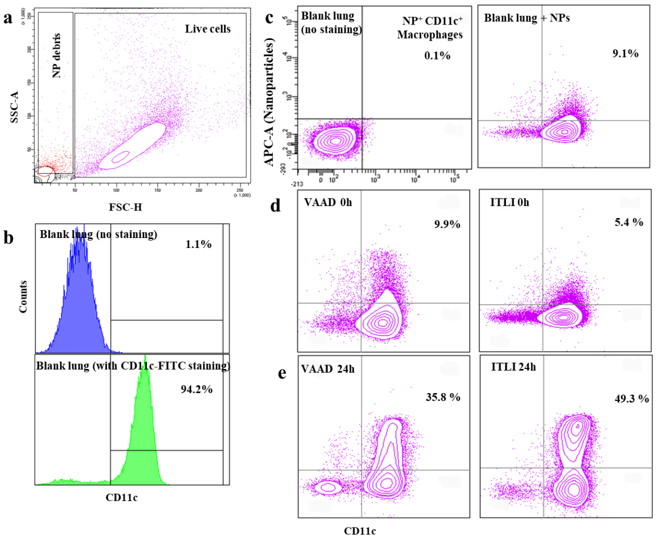

Figure S11: Flow cytometry gating strategy for NP^{+} Cd11c^{+} BAL cells obtained from 24h post VAAD and ITLI deliveries.

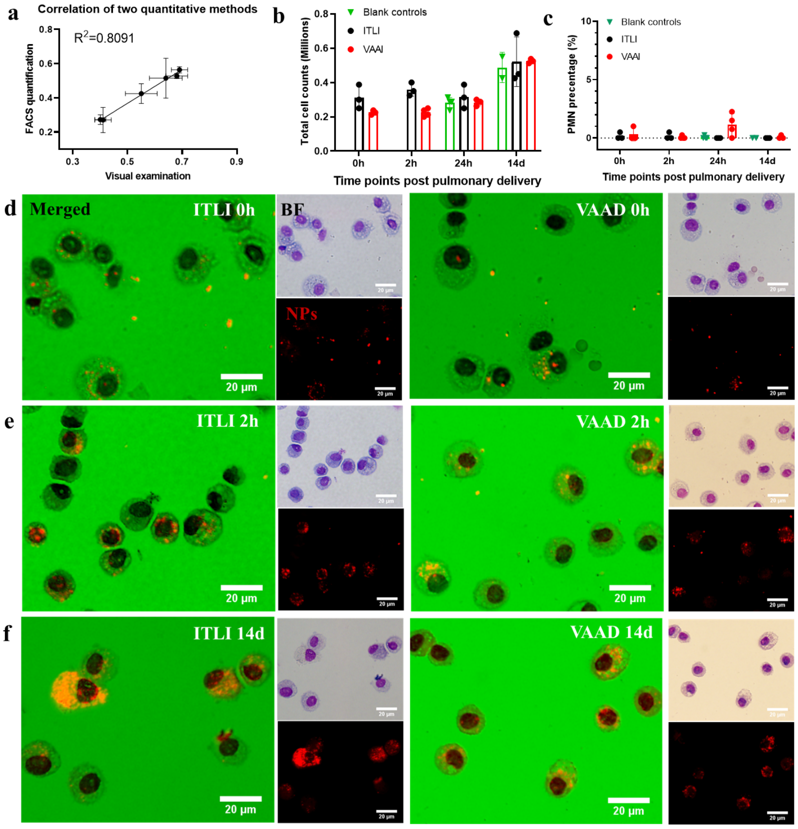

Figure S12: Determination of lung inflammation and NP quantification in BAL cells obtained from WT mice post 24h ITLI administration. a) Correlation of two quantitative methods (visual examination and FACS quantification) for detection of NP^+ macrophages in BAL fluid. b and c) total cell count and PMN cell count at four time points post VAAD and ITLI deliveries. d, e, and f) representative BAL cell images comprise both bright-field images (Grünwald-Giemsa stained) and fluorescence of NPs at 0h, 2h, and 14d post VAAD and ITLI deliveries.

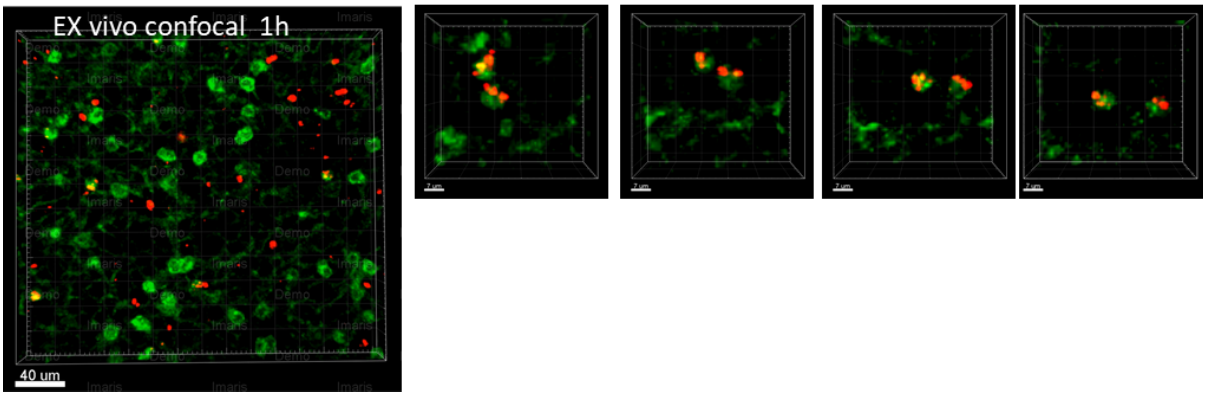

Figure S13: *Ex vivo* lung living microscopy depicted the migration of GFP-expressing, NP-laden macrophages in the PCLS punches within 18h after ITLI administrations using laser scanning confocal microscopy.

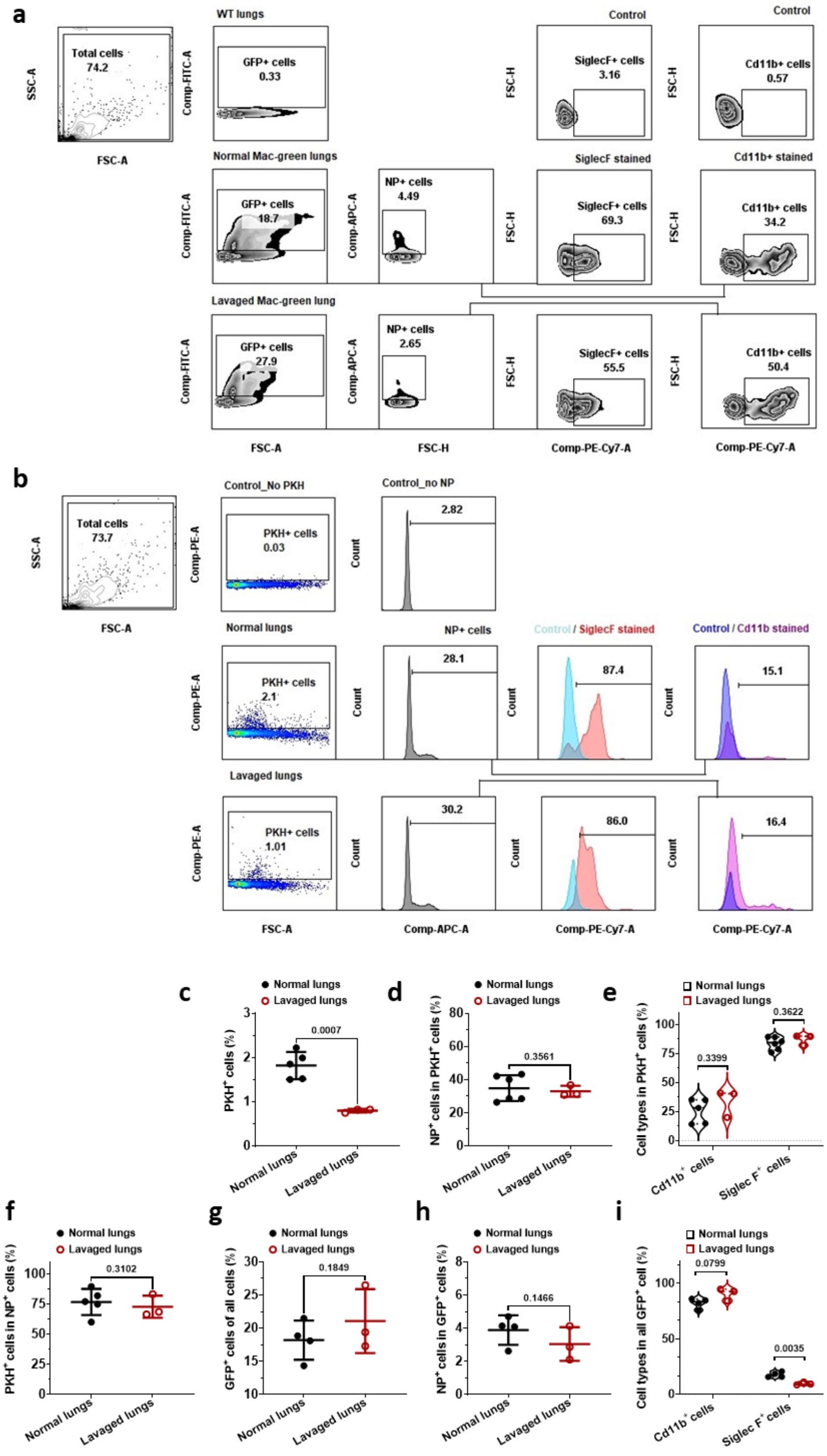

Figure S14: Flow cytometric analysis and quantification of SiglecF$^+$ or Cd11b$^+$ macrophages in normal and lavaged WT and Mac-green mice. a) schematic illustration of cell-population analysis for GFP-expressed, NP-laden macrophages in normal and lavaged Mac-green mice groups. b) schematic illustration of cell-population analysis for PKH stained, NP-laden macrophages in normal and lavaged WT and Mac-green mice groups. c-i) Quantification of multiple cell populations in PKH$^+$ or GFP$^+$ cells in normal and lavaged lung cells.

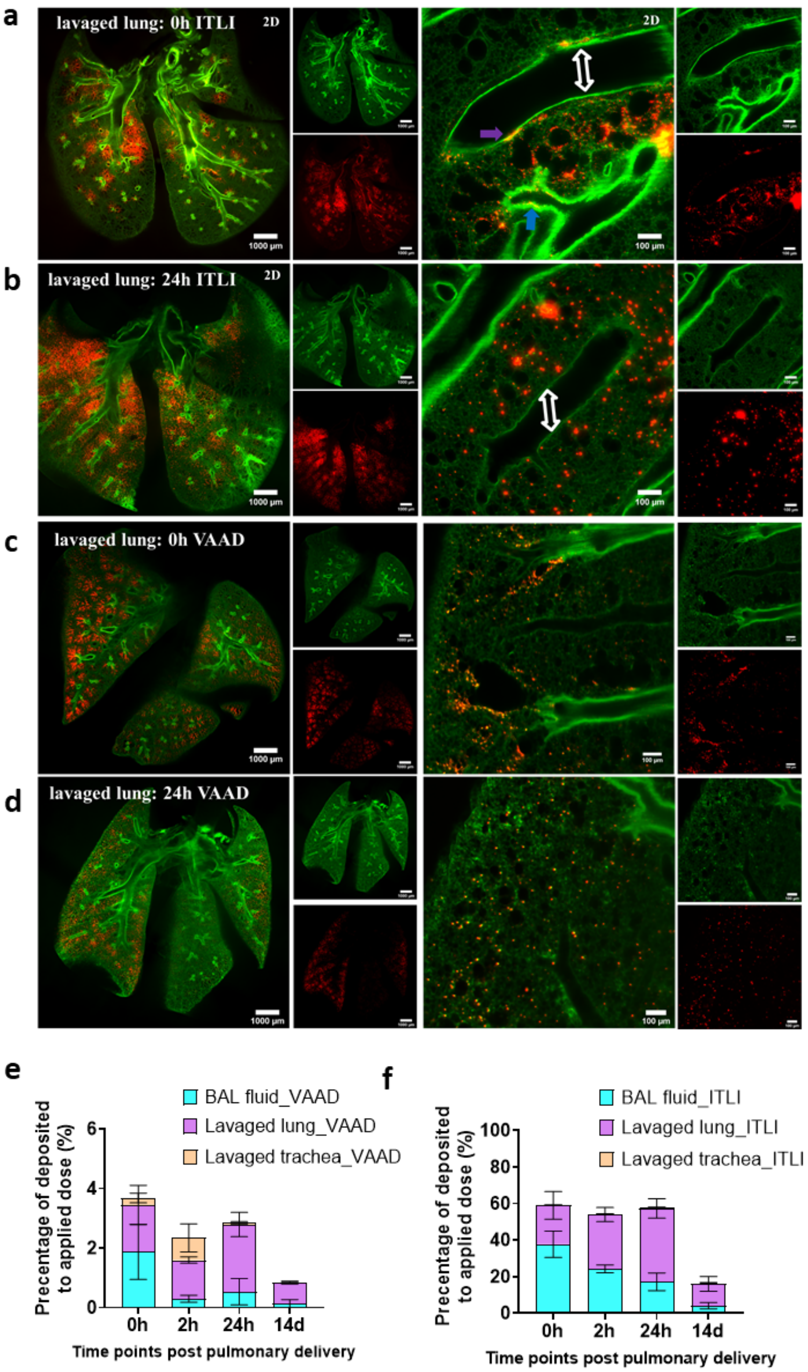

Figure S15: Single-slice view of lavaged lungs of mice post 0h and 24h of VAAD and ITLI administrations (a-d, double-sided arrows indicated blood vessels, purple referred to NPs close to the endothelium) and the percentage of deposited to applied doses in different lung compartments (BAL fluid, lavaged lungs, and lavaged trachea, e and f).

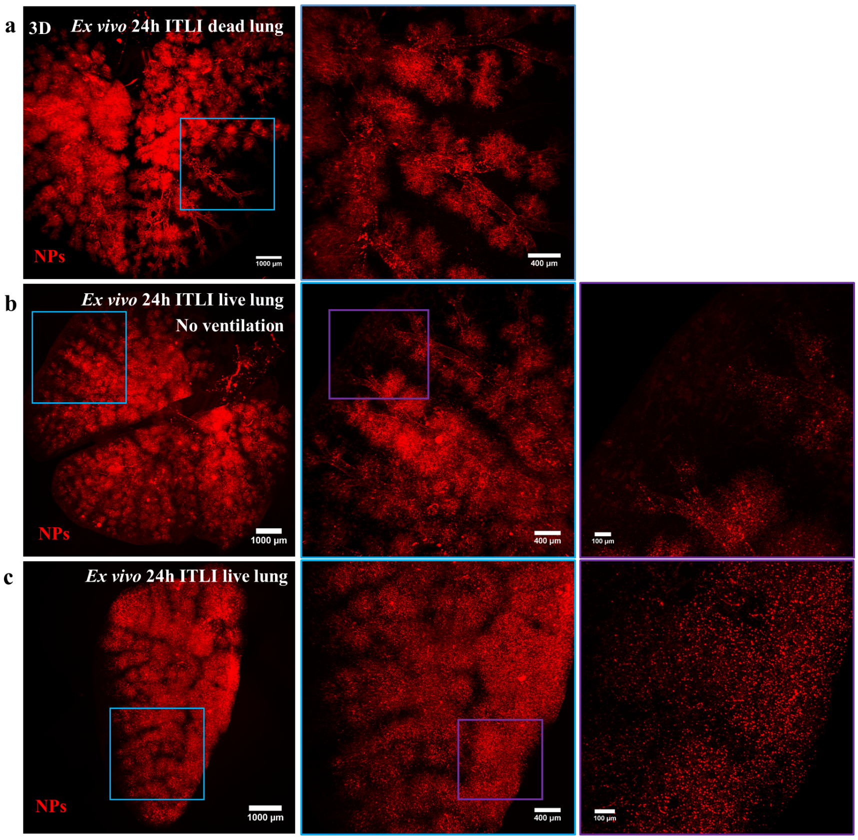

Figure S16: Single-channel 3D view of NP whole-lung distribution/deposition pattern in *ex vivo* ITLI lungs post PFA fixation or PBS incubation and *ex vivo* ventilation. The lungs were instilled with MF and isolated from the mice immediately, and were then subjected to either the PFA fixation (a and b) or PBS incubation (c) for 3-4h and 24h *ex vivo* physiological ventilation (no ventilation for b).

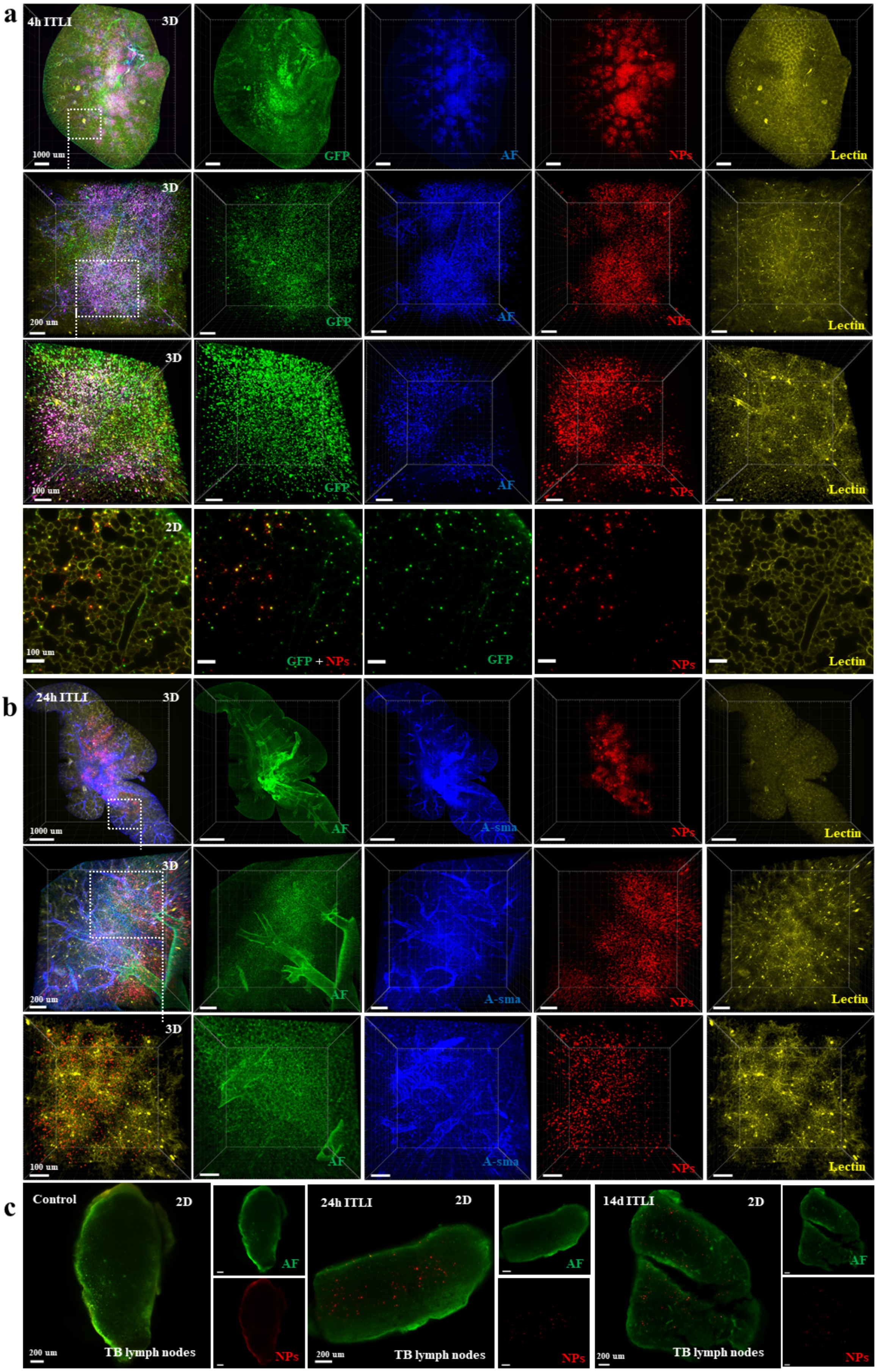
a
4h ITLI
3D
1000 um
GFP
AF
NPs
Lectin
3D
200 um
GFP
AF
NPs
Lectin
3D
100 um
GFP
AF
NPs
Lectin
2D
100 um
GFP + NPs
GFP
NPs
Lectin
b
24h ITLI
3D
1000 um
AF
A-sma
NPs
Lectin
3D
200 um
AF
A-sma
NPs
Lectin
3D
100 um
AF
A-sma
NPs
Lectin
c
Control
2D
200 um
TB lymph nodes
AF
NPs
24h ITLI
2D
200 um
TB lymph nodes
AF
NPs
14d ITLI
2D
200 um
TB lymph nodes
AF
NPs

Figure S17: Merged and single channel 3D and 2D views of NP distribution with multiple lung networks. a)multiple magnification observations of NP distribution, macrophages, and lectin-labeled capillary network in an entire lung lobe of transgenic GFP-expressed mouse (CSF1R-GFP positive macrophages/monocytes). b) multiple magnification observations of NP distribution, lectin-labeled vasculature, and alpha-sma labeled network in an entire lung lobe of a wildtype mouse. c) 2D sections of tracheobronchial lymph nodes obtained from blank mice or 24h and 14d ITLI exposed mice.